Unloaded Speed of Shortening in Voltage-Clamped Intact Skeletal Muscle Fibers from wt, mdx, and Transgenic Minidystrophin Mice Using a Novel High-Speed Acquisition System

O. Friedrich,* C. Weber,* F. v. Wegner,* J. S. Chamberlain,† and R. H. A. Fink*

*Medical Biophysics, Department of Systems Physiology, Institute of Physiology and Pathophysiology, Ruprecht-Karls-University, Heidelberg, Germany; and †Department of Neurology, University of Washington, Seattle, Washington

ABSTRACT Skeletal muscle unloaded shortening has been indirectly determined in the past. Here, we present a novel high-speed optical tracking technique that allows recording of unloaded shortening in single intact, voltage-clamped mammalian skeletal muscle fibers with 2-ms time resolution. L-type Ca^{2+} currents were simultaneously recorded. The time course of shortening was biexponential: a fast initial phase, τ_1, and a slower successive phase, τ_2, with activation energies of 59 kJ/mol and 47 kJ/mol. Maximum unloaded shortening speed, $v_{u,max}$, was faster than that derived using other techniques, e.g., $\sim$14.0 $L_0\,s^{-1}$ at 30°C. Our technique also allowed direct determination of shortening acceleration. We applied our technique to single fibers from C57 wild-type, dystrophic mdx, and minidystrophin-expressing mice to test whether unloaded shortening was affected in the pathophysiological mechanism of Duchenne muscular dystrophy. $v_{u,max}$ and $a_{u,max}$ values were not significantly different in the three strains, whereas τ_1 and τ_2 were increased in mdx fibers. The results were complemented by myosin heavy and light chain (MLC) determinations that showed the same myosin heavy chain IIA profiles in the interossei muscles from the different strains. In mdx muscle, MLC-1f was significantly increased and MLC-2f and MLC-3f somewhat reduced. Fast initial active shortening seems almost unaffected in mdx muscle.

INTRODUCTION

Skeletal muscle contraction is the mechanical result of a complex cascade of signaling events (e.g., (1–3)) that finally triggers actomyosin cross-bridge cycles (4–6). Force production and fiber shortening are primarily determined by external load conditions with purely isometric and isotonic contractions at both ends of the spectrum (7). The maximum rate of shortening in single fibers occurs under unloaded conditions and correlates with motility assay data from isolated motorproteins (8,9). During unloaded shortening, weakly attached cross-bridges are preferentially recruited, with strongly attached ones being as low as 1–5%, whereas strongly attached cross-bridges are formed when the external load increases (10). Maximum unloaded speed of shortening ($v_{u,max}$) highly depends on distributions of myosin heavy chain (MHC), light chain (MLC), and myosin ATPase activity (11–13). The myosin composition is particularly variable in different muscle types, and even within the same muscle, under different developmental, neural, hormonal, aging, or disease states, fiber type changes may occur (14–16). Likewise, MLC phosphorylation is known to modulate shortening velocity (17).

Previous studies of unloaded speed of shortening in skeletal muscle primarily relied on two experimental approaches: force-velocity relationships and ''slack-test'' methods. The first uses the fact that speed of shortening critically depends on external load. After isometric contraction against an external load, shortening velocity is measured in the ensuing isovelocity phase and $v_{u,max}$ is usually indirectly extrapolated from the hyperbolic force-velocity relation toward zero loads (e.g., (18–20)). However, this value is not unproblematic, as $v_{u,max}$ may be underestimated by deviations of the force-velocity data from the hyperbolic Hill function for very heavy and light loads (20,21). The ''slack-test'' method assumes a phase of constant velocity during unloaded shortening while taking up a slack length (22,23). There have been considerable deviations of $v_{u,max}$ obtained from both methods (22,24), in both intact and skinned fibers, that may be due to experimental uncertainties in resolving slack times from the force traces or using different fitting procedures (20,25). Also, the concept of isovelocity phases in intact muscle fibers under conditions of maximum Ca^{2+}-induced shortening might be questionable. Instead, velocity can be expected to change in a nonlinear fashion by the underlying cross-bridge kinetics and opposing forces from elasticity elements or friction from external environments. A more direct experimental approach to visualize depolarization-induced shortening in intact fibers would provide useful insights into single-fiber mechanics under more physiological conditions or to explore pathophysiological mechanisms of muscle diseases that may affect contractility.

In Duchenne muscular dystrophy (DMD), the 427-kDa protein dystrophin is absent due to different deletions in the dystrophin gene (e.g., (26)). Dystrophin mechanically links the

Submitted November 27, 2007, and accepted for publication February 8, 2008.

Address reprint requests to O. Friedrich, Medical Biophysics, Dept. of Systems Physiology, Institute of Physiology and Pathophysiology, Ruprecht-Karls-University, INF 326, 69120 Heidelberg, Germany. Tel.: 49-6221-54-4143; Fax: 49-6221-54-4123; E-mail: oliver.friedrich@physiologie.uni-heidelberg.de.

O. Friedrich is both first and senior author.

Editor: K. W. Ranatunga.

0006-3495/08/06/4751/15 $2.00

doi: 10.1529/biophysj.107.126557

cytoskeleton to the extracellular matrix and provides mechanical stability and positioning of single fibers within the matrix (27,28). The mechanism leading to progressive weakness is not understood in detail but involves aberrant mechanotransduction (29), altered Ca^{2+} homeostasis (30–32), or ion channels (33,34). As is the case in DMD patients, muscles from mdx mice, the animal model for DMD (35,36), show increased contraction-induced damage (37,38) and significantly decreased isometric force (39–41). In diaphragm muscle strips of 6-month-old mdx mice, an additional marked reduction in $v_{u,max}$ from force-velocity relationships, a decrease in slow myosin isoforms, and an increase in IIA MHC isoforms were found, and it was hypothesized that lack of dystrophin might additionally result in molecular motor dysfunction, at least in diaphragm muscle (41). However, there are still no data about unloaded speed of shortening in mdx hindlimb muscle fibers (36). Mechanical parameters, i.e., isometric force and power output, have been a sensitive diagnostic tool to test the efficiency of gene therapy strategies, e.g., using mini- or microdystrophin expression in mdx mice (42,43) that can potently restore force (44). Their effects on unloaded speed of shortening have not been assessed yet.

In this study, we introduce what to our knowledge is a new high-speed line-scan technique to monitor the time course of fiber length, $l(t)$, during unloaded shortening under defined intracellular voltage-clamp conditions in single intact muscle fibers with a time resolution of 2 ms. Simultaneously, slowly-activating Ca^{2+} currents (i_{Ca}) during maintained depolarizations were recorded. $v_{u,max}$ seems to be considerably faster than that estimated using previous methods, described above. We show that unloaded speed of shortening is unaltered in mdx fibers.

Preliminary results were presented at the European Muscle Conference 2005 in Debrecen, Hungary (45).

METHODS

Preparation

Adult male BALB/c mice 12–14 weeks old were sacrificed by exposure to an overdose of CO_2 atmosphere. All experiments were carried out according to the guidelines laid down by the local Animal Care Committee. Interossei muscles were dissected in isotonic Ringer's solution (see below) and enzymatically isolated as previously described (33,46). The BALB/c strain was initially used to establish the fast-fiber-length tracking system and to investigate the temperature dependence of the contraction kinetics under voltage-clamp conditions. In a subsequent setting of experiments, the influence of dystrophin on the contraction kinetics under the same conditions was studied. For this, fast-fiber-length recording was applied to single fibers from adult wt C57/SV129, dystrophic mdx, and transgenic minidystrophin (MinD)-expressing, middle-aged mice (8–12 months). MinD mice are a transgenic strain with the mdx background (CVBA3′, 43) that express the Δexon17–48 mouse minidystrophin construct with a molecular mass of 228 kDa (43,43).

Solutions

Ringer's solution contained (in mM) 136 NaCl, 4 KCl, 2 $CaCl_2$, 1 Mg acetate, 5 glucose, and 10 HEPES, pH 7.4. For maximum mechanical activation of single muscle fibers under voltage-clamp conditions, a 10-mM free-Ca^{2+}-containing isotonic solution for simultaneous recordings of slow L-type calcium currents (i_{Ca}) was used (mM): 10 Ca-acetate, 1 Mg acetate, 146 TEA-Br, 10 HEPES, 5 CsBr, 5 4-aminopyridine, 5 3,4-di-aminopyridine, and 5 glucose. The ionic strength ($\Gamma/2$ values) of this solution was calculated to 184 mM and had a measured osmolarity of 338 mOsm l^{-1}. Protein extraction buffer contained (in mM) 300 NaCl, 100 NaH_2PO_4, 50 Na_2HPO_4, 10 $Na_4P_2O_7$, 1 $MgCl_2$, 10 EDTA, and 1.4 β-mercaptoethanol, pH 6.5.

Electrophysiology

For mechanical activation of single intact interossei fibers and recording of i_{Ca}, the two-microelectrode voltage-clamp technique was applied as previously described (33,46–48). To maximally activate both fiber shortening and i_{Ca}, step pulses to 0 mV were applied for 1 s from a holding potential of −70 mV under isotonic external conditions. Linear currents were subtracted using an analog leak subtraction procedure (33,47,48). A pulse to 0 mV was chosen because the i_{Ca}-V curve usually has its maximum close to 0 mV (e.g., (33,46,47)). In some fibers, a second pulse could be applied to +10 mV after having recovered from the 0-mV pulse, with no apparent further change in shortening parameters such as maximum shortening velocity or shortening length (not shown). Therefore, a pulse to 0 mV was well considered to maximally activate fiber shortening. For better comparison between different fibers, the current density, I_{Ca}, was calculated by normalizing i_{Ca} to the membrane surface assuming cylindrical fiber geometry, as described previously (e.g., (33,46)). The fiber dimensions were taken from optical measurements in isotonic Ringer's solution. From I_{Ca} recorded during the maintained 1-s depolarizing pulse, the I_{Ca}-induced rise in myoplasmic $[Ca^{2+}]_i$ (i.e., additional to the Ca^{2+} release from the sarcoplasmic reticulum (SR)) was calculated by integration with respect to time. Note that the SR Ca^{2+} release itself could not be resolved using the current technique.

High-speed line-scan recording of fiber length during shortening

A b/w linear charge-coupled device (CCD) line (ILX26A, Sony, San Diego, CA) was integrated into a custom-built line-scan unit and connected to the optical side port of an inverse microscope (IMT-2, Olympus, Melville, NY). The maximum internal pixel sampling rate of the CCD line was 1 MHz, with a sensitivity of 300 $Vlux^{-1}$ s^{-1}. The line-scan recording could be started by an external TTL trigger pulse. Maximum sampling rate was 2 ms/line. This maximum scan frequency (500 Hz/line) was a compromise between the sampling rate of the acquisition board and the aim to trace the whole fiber length within a 512-pixel cycle at the given objective magnification (A10 PL 0.25 or ULWD CDPlan20 0.4, Olympus). Thus, a recording cycle of the actual fiber length was accomplished every 2 ms. The TTL trigger unit was further connected to the A/D-board (DigiData 1200 B, Axon Instruments, Foster City, CA) of the two-microelectrode voltage-clamp setup to start the step-pulse depolarization and i_{Ca} recording simultaneously with the fiber-length recording by application of a 100-μs TTL pulse (Fig. 1). To further validate the accuracy of our high-speed line-scan recordings, in some experiments fiber shortening was simultaneously recorded with a 25-Hz CCD camera (DXC-107P, Sony). Fig. 1 shows a schematic diagram of the experimental setup.

Temperature control unit

The temperature of the experimental chamber was controlled by four liquid-cooled DC-driven Peltier elements. Temperature was adjusted by an analog feedback loop, including a thermosensor placed in the metal block containing the recording chamber. The thermosensor and the Peltier elements were electrically uncoupled to reduce noise to the voltage-clamp recording. Temperature was controlled with an accuracy of ±0.1°C and experiments were performed at different temperatures between 10°C and 30°C.

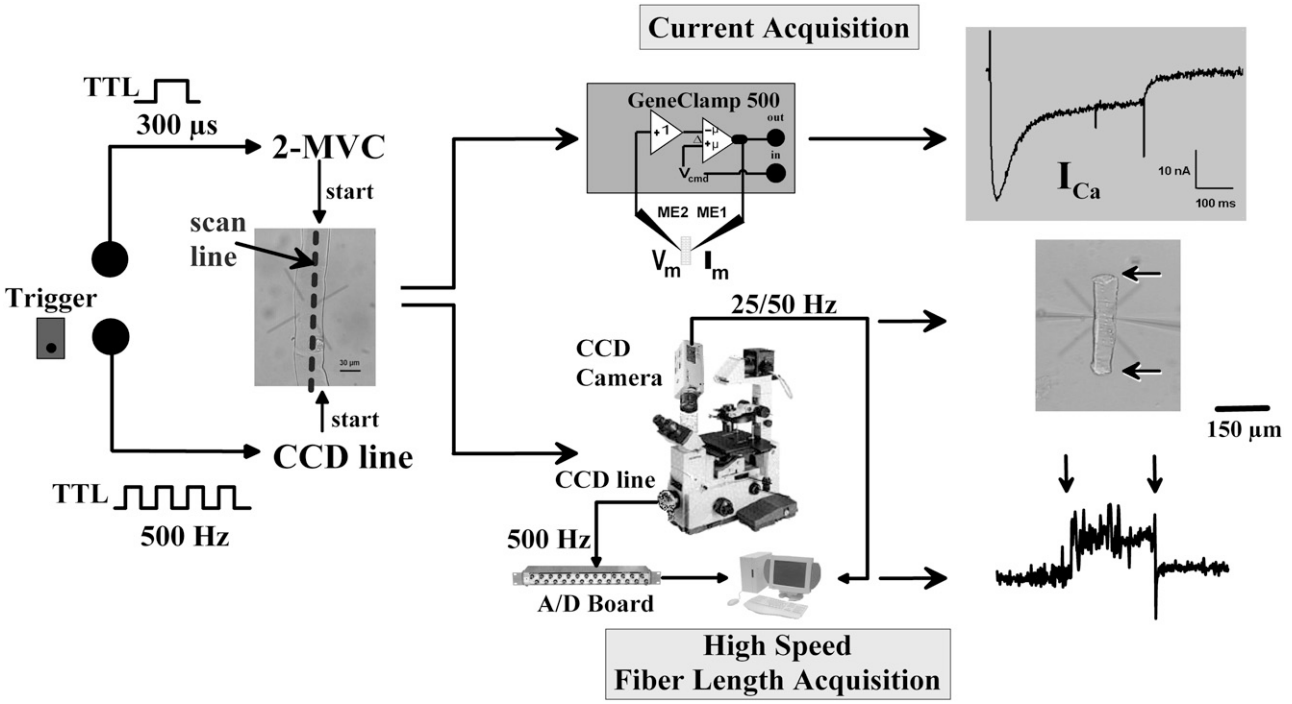

FIGURE 1 Schematic diagram of the experimental setting for simultaneous recordings of I_{Ca} and fiber length $l(t)$ during unloaded shortening. A manually elicited TTL trigger pulse is sent to the voltage clamp unit that starts intracellular stimulation (a 1-s depolarizing pulse to 0 mV) and recording of I_{Ca}. At the same time, a repetitive 500-Hz TTL pulse is applied to drive the CCD line. The line-scan signal is acquired via the A/D board and stored on the hard disk. In some experiments, a commercial 25-Hz CCD camera was used to simultaneously record the video sequence of fiber shortening.

Experimental procedure

Single fibers were transferred to the recording chamber and inserted into the thermoblock. The desired temperature was set and ~5 min allowed for temperature equilibration. Microelectrodes were filled with 3 M KCl and positioned close to the fiber ends. The CCD-line axis was then adjusted until it matched the fiber axis. The correct position of the CCD line was verified by the appearance of a sharp voltage spike on an external oscilloscope (HM205-3, Hameg, Frankfurt, Germany) that reflected the position of the microelectrodes close to the fiber ends. The microelectrodes were then repositioned and inserted in the middle of the fiber, perpendicular to the fiber axis. This configuration allows shortening of the fiber and eliminated contraction-induced damage to the membrane (33,46,47). The holding potential was quickly adjusted to −70 mV and the fiber was depolarized by manually eliciting a TTL trigger pulse that started simultaneous recording of membrane currents and fiber length by the CCD line via two acquisition PCs (see Fig. 1).

Data acquisition and analysis

Fiber-length traces $l(t)$ were recorded and analyzed using AxoTape 2.0 (Axon Instruments). i_{Ca} were recorded using pClamp6 and pClamp8 software (Axon Instruments). The signal from the CCD-line output represents a voltage signal over a time period of 2 ms/frame (512 pixels, see Fig. 2 *A*). The apparent fiber length in a frame was manually evaluated by following the sharp voltage peaks (i.e., representing the change in contrast of transmitted light at the fiber ends) at the margin of successive frames. Using this method, the fiber edges could be reliably detected in each frame. The change in fiber length was calculated between successive frames, resulting in the time course of fiber length $l(t)$ with a 2-ms resolution ($l(t + 2$ ms)). The peak-to-peak interval in each frame was converted to apparent fiber length using a calibration grate. Usually, $l(t)$ was expressed as a percentage of the initial fiber length, L_0, to compare data between different fibers. The time course of the shortening velocity $v(t)$ and shortening acceleration $a(t)$ were obtained by differentiating $l(t)$. To preserve the resolution of the $l(t)$ data, a single-step-forward differential was built between each time point t_i and t_{i+1} (with $t_{i+1} - t_i = 2$ ms). It should be noted that due to the discrete digitization of the line-scan intervals, the $v(t)$ and $a(t)$ data are also discrete (see, e.g., Figs. 5 and 6) and the error of their extracted maximum values is represented by the smallest discrete step. This error has been acknowledged in the statistics of mean values of $v(t)$ and $a(t)$. Other attempts to reduce the discrete step values included the use of a symmetrical forward backward differential (t_{i-1} and t_{i+1}) and a five-point environment (t_i and $t_{i\pm2}$, not shown). However, all these approaches resulted in discrete averaging and a marked reduction in apparent $v(t)$ and $a(t)$, as would be expected by a smoothing procedure of the data. Therefore, the $l(t)$ data were processed unfiltered and the values for maximum shortening velocities, $v_{u,max}$, and acceleration, $a_{u,max}$, can be regarded as an upper limit at the given acquisition rate.

Fig. 2 *A* shows the CCD line-scan data for a single BALB/c fiber bathed in isotonic 10 mM Ca^{2+} solution at 30°C that was activated by a step pulse to 0 mV. From the 500 frames of the 1-s lasting pulse, only a few are shown at the times indicated. The peak-to-peak times were measured (*arrow lengths*) and the resulting fiber lengths calculated as described above. To minimize errors in resting fiber lengths determined from the line-scan signal with respect to optically measured resting lengths from the same fiber, care was taken to select fibers with almost no curvature for the current experiments (see Appendix). Fig. 3 shows an example of such a single fiber (see Appendix for details).

Video data from the CCD camera were stored on a PC using a frame grabber card (Matrox Meteor). To increase the time resolution of the 25-Hz video signal to 50 Hz, a Pascal-routine was written to split half-frames by selecting odd and even lines of the full-frame image. Fig. 2 *B* shows a selection of video frames from another shortening fiber at 30°C depolarized to 0 mV for 1 s. Fiber length was measured using the imaging software Scion Image (Scion Corporation, Frederick, MD) and Image J (National Institutes

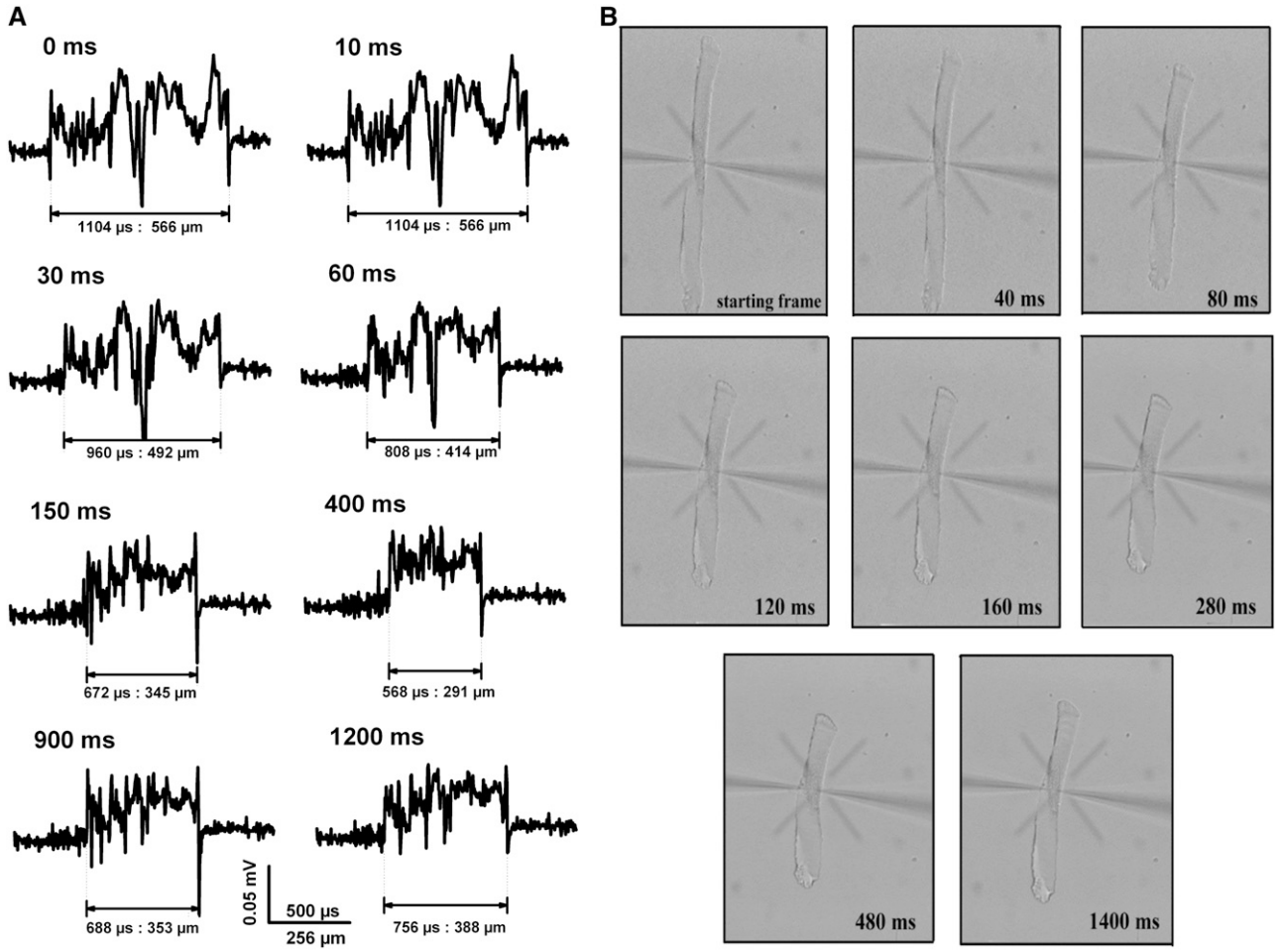

FIGURE 2 Line-scan recordings of the fiber length, $l(t)$, during contraction and shortening under maintained depolarization in single fibers. (*A*) The selection shown is from the shortening sequence of a representative single BALB/c fiber recorded with the CCD line at 500 Hz during a maintained 1-s depolarization to 0 mV from a holding potential of −70 mV at 30°C (identifier D27020.dat). Arrows mark the area between the fiber edges within the actual frame, given as elapsed scan time in the raw data and converted to absolute fiber length as described in Methods. The resting fiber length of $L_0 = 566 \pm 6$ μm at $t = 0$ ms from the line-scan data corresponded well with the value of $L_0 = 560 \pm 10$ μm optically measured using a microscope scale. (*B*) A selection of the shortening sequence recorded with the video camera after separation of half-frames (50 Hz) from another single fiber under the same conditions as in *A*. The fast initial shortening can only be resolved at 40-ms intervals (full frames) in *B*, whereas temporal resolution is 20 times faster in *A*.

of Health software). Data were analyzed using SigmaPlot 9 (Systat Software, San Jose, CA) and Origin 6 (Microcal, Northampton, MA). Data are presented as mean ± SE, with the number of observations, *n*. A Grubbs test was performed on data sets to identify outliers at the $P = 0.05$ level. Temperature dependence of shortening kinetics was either expressed as Q_{10} values or calculating the activation energy E_a (where applicable) from the slope of the Arrhenius plots of the kinetics parameters. Statistical differences between temperature groups within one strain or differences between strains at a given temperature were detected by one-way ANOVA or pairwise multiple comparison procedures (Holm-Sidak method), where appropriate. $P < 0.05$ was considered significant.

Sodium dodecyl sulfate MHC and MLC protein quantification in wt, mdx, and MinD interossei muscles

To quantify the protein contents and distribution of MHC and MLC in interossei muscles from wt, mdx, and MinD mice, sodium dodecyl sulfate polyacrylamide gel electrophoresis (SDS-PAGE) was performed (49). Extensor digitorum longus (EDL) and soleus muscle from wt mice were also used for comparison. After dissection of small fiber bundles containing ~15 fibers, myosin was extracted at room temperature for 30 min in protein extraction buffer (see Solutions), centrifuged, mixed 1:2 with standard protein buffer, and added (~10 μl) to the running gel (49). The total protein content added to the gels was estimated to be ~100–200 μg. MLC and MHC gels were run from the same supernatant each. The separating and stacking gels, as well as the separating and running buffer, were composed according to Agbulut et al. (50). MHCs were separated on 8% polyacrylamide gels (50) and MLCs on 12% gels (49). A standard Coomassie blue staining was performed. Broad-range protein standards were from BioRad Laboratories (Munich, Germany). Protein gels were scanned and analyzed using AIDA software (Raytest, Straubenhardt, Germany). For evaluation of the fast myosin light chain isoform (MLC-1f, MLC-2f, and MLC-3f) mean protein densities in the three genotypes (wt, MinD, and mdx), the area under the corresponding peaks in density profiles of the background normalized bands from up to nine gels were measured and the relative percentage calculated (MLC-1f + MLC-2f + MLC-3f adding up to 100%).

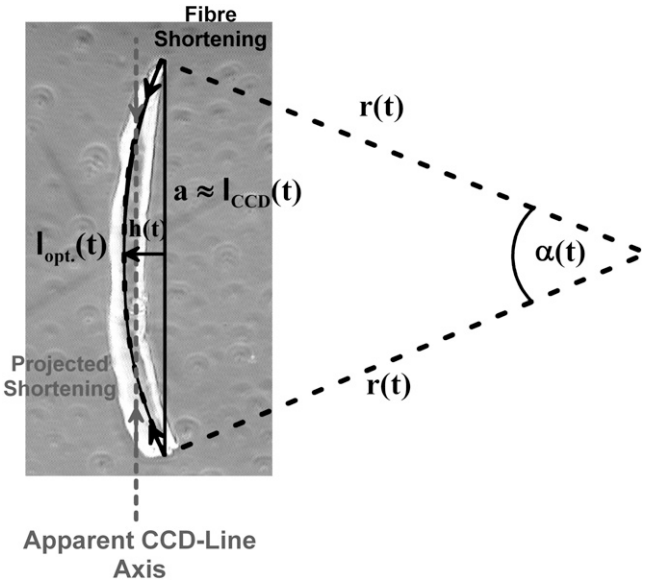

FIGURE 3 Single-fiber geometry and relative CCD line orientation used to estimate the error of fiber shortening recorded with the 500-Hz line-scan device. Example of a single fiber with a curvature. The trajectory of the fiber axis deviates from the linear CCD array at the fiber endings. The arc of the imposed fiber radius is used to estimate the error introduced in obtaining $v_{u,max}$ from the CCD-line data. As derived in the Appendix, $v_{u,max}$ is even underestimated in curved fibers. Care was taken to select fibers with a minimum curvature introducing <5% errors.

RESULTS

Simultaneous recording of $l(t)$ and I_{Ca} under maintained depolarization to 0 mV at different temperatures

Fig. 4 *A* shows the time course of shortening $l(t)$ normalized to the resting fiber length L_0 during a 1-s depolarizing pulse to 0 mV in a representative single BALB/c muscle fiber recorded with the CCD line (500 Hz) at 30°C. A latency of ~16 ms for the onset of shortening can be seen at the beginning of the recording that was similar in several fibers and not temperature-dependent ($P > 0.1$, Table 1). This latency represents the time required for excitation-contraction coupling (i.e., SR Ca^{2+} release and myoplasmic diffusion) and is ~20 ms (51). It is followed by a fast contractile activation phase and a slow relaxation phase. The first 50 ms of the contractile activation are shown on an extended timescale in the inset of Fig. 4 *A*. In the example shown, shortening is complete after ~400 ms at ~50% of L_0. The shortening phase was best described by a double exponential fit:

$$l(t)_{\text{shortening}} = A_1 \times e^{-\frac{t}{\tau_1}} + A_2 \times e^{-\frac{t}{\tau_2}} + const, \qquad (1)$$

with a fast time constant τ_1 and a slow component τ_2, measuring 13.6 ms and 133 ms, respectively. The much slower relaxation phase was best described by a single exponential with a time constant τ_3 of 678 ms. As the relaxation phase was very variable between fibers, even at the same temperature, we focused on the more interesting fast activation phase where both shortening velocity and acceleration had their maximum. Therefore, τ_3 values are not further analyzed here. Note that the relaxation phase of the fiber took place while the fiber was still being depolarized by the 1-s pulse to 0 mV. At lower temperatures, relaxation was not yet fully present during the recording interval (e.g., Fig. 4, *B* and *C*). Table 1 summarizes the mean values for the onset latency: minimum fiber length l_{min}/L_0; the time to minimum (TTM); maximum unloaded speed of shortening, $v_{u,max}$; and time to $v_{u,max}$, TT$v_{u,max}$ (see below) in several single BALB/c fibers at four different temperatures. Note that at 24°C, values from BALB/c and C57 wt single fibers were lumped together, as they were similar. The mean amplitudes of the exponential fits showed a tendency to increase with temperature for A1 (0.26 ± 0.06 at 10°C, 0.12 ± 0.02 at 20°C, 0.46 ± 0.08 at 24°C, and 0.90 ± 0.42 at 30°C) that was, however, not statistically significant ($P = 0.1$). For A2, values ranged from 0.03 to 0.52 and were only significantly smaller at 10°C compared to larger temperatures ($P < 0.01$).

In some experiments, in addition to the line scan, $l(t)$ was also recorded with an untriggered video camera. The minimum fiber length during shortening and its time course were very similar with both techniques (data not shown). Therefore, like the video sequence, the CCD line faithfully tracks $l(t)$, but with at least 10-fold higher time resolution.

Simultaneous with the fast $l(t)$ recordings, L-type i_{Ca} were recorded. Fig. 4 *B* shows $l(t)$ in another single BALB/c fiber recorded at 24°C together with the time course of i_{Ca}, given as surface normalized I_{Ca} (Fig. 4 *B*, *inset*, *solid line*). Also shown is the calculated I_{Ca}-induced rise in intracellular $[Ca^{2+}]_i$ during the maintained depolarizing pulse, $[Ca^{2+}]_i$ (I_{Ca}), that results in an increase in $[Ca^{2+}]_i$ of ~70 μM by the end of the pulse. It should be noted that $[Ca^{2+}]_i$ (I_{Ca}) reflects the contribution from Ca^{2+} influx through dihydropyridine receptors (DHPRs) under this maintained depolarization condition and not the contribution from sarcoplasmic reticulum (SR) Ca^{2+} release. Therefore, the increase in $[Ca^{2+}]_i$ under voltage-clamp conditions is much larger than under single-twitch conditions (~20 μM (52)), where only SR Ca^{2+} release contributes and DHPRs in skeletal muscle do not reach a fully conducting state (53). On the other hand, this increase, in addition to the Ca^{2+} release from the SR during activation, ensures Ca^{2+}-saturated conditions of the contractile apparatus and, therefore, maximum mechanical activation (see also below). In the example shown, peak I_{Ca} was −51.9 μA/cm^2 and time to peak (TTP) was 47.5 ms. The peak I_{Ca}, TTP, and $[Ca^{2+}]_i$ (I_{Ca}) values at the end of the pulse (1 s) and at the time of maximum unloaded speed of shortening, TT$v_{u,max}$ (see below), for several single BALB/c fibers at 10°C, 20°C, 24°C, and 30°C are summarized in Table 2. The I_{Ca} data confirm our previous data carried out at room temperature under isotonic conditions (33,46). At 30°C, an early outward component of I_{Ca} was occasionally seen during the current decay after the I_{Ca}

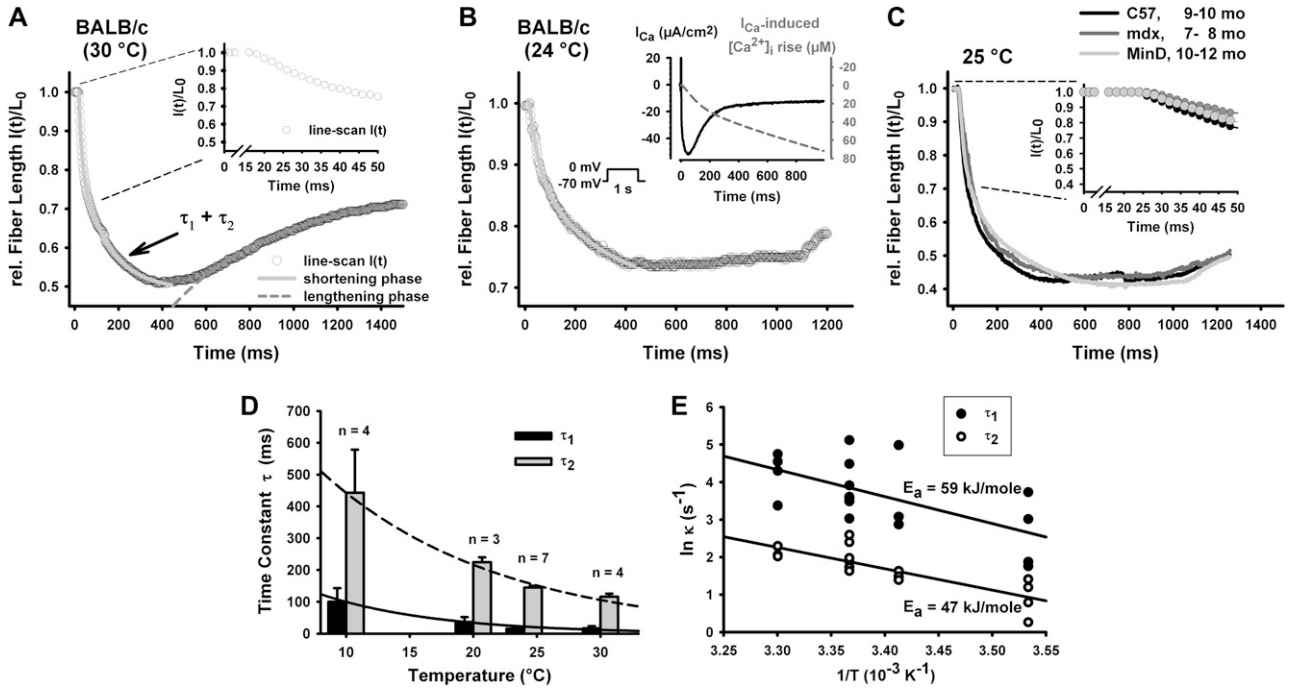

FIGURE 4 Kinetics of unloaded shortening $l(t)$ during maintained depolarizations in single fibers. (*A*) Representative recording of $l(t)$ with the line scan (500 Hz) in a single BALB/c fiber at 30°C. A biexponential shortening phase with time constants τ_1 and τ_2 and a single-exponential relaxation phase can be distinguished during the 1-s lasting depolarizing pulse from −70 mV to 0 mV. The early transient of $l(t)$ is shown on an extended timescale (0–50 ms) in the inset. Shortening starts after an onset latency of ~16 ms in the fiber shown. (*B*) Sample recording of $l(t)$ in another BALB/c fiber at 24°C. The time course of the simultaneously recorded I_{Ca} and the calculated I_{Ca}-induced rise in intracellular $[Ca^{2+}]_i$ is shown in the inset. (*C*) $l(t)$ recorded with the line scan in a representative adult single wt, mdx, and MinD fiber at 25°C. The first 50 ms of shortening are shown in the inset on an extended timescale. (*D* and *E*) Exponential temperature dependence of both τ_1 and τ_2 (*D*) and Arrhenius plot of both shortening rate constants with the calculated activation energy as indicated (*E*).

peak (46). This component obviously reduces $[Ca^{2+}]_i$ (I_{Ca}) so that the corresponding values in Table 2 at 30°C might be somewhat underestimated. Q_{10} values for peak I_{Ca} were close to unity between 10°C and 20°C and ~2 between 20°C and 30°C. I_{Ca} activation was most prominently affected by an almost fourfold decrease of TTP between 20°C and 30°C.

Fig. 4 *C* shows representative examples of $l(t)$ traces from adult single C57 wt, mdx, and MinD fibers of similar aged animals (8–12 months), each recorded during a maintained depolarization to 0 mV at 24°C. The more interesting fast-activation phase is again shown on an extended timescale in the inset. Shortening was very similar in all three genotypes. A more detailed analysis is given in the sections below.

The temperature dependence of the time constants of the shortening phase, τ_1 and τ_2, are evaluated for all BALB/C fibers (including some wt fibers at 24°C) in Fig. 4 *D*. The temperature dependence was exponential for both time constants. From the Arrhenius plot of τ_1 and τ_2, the activation energy E_a was calculated at 59 kJ/mol and 47 kJ/mol, respectively (Fig. 4 *E*).

Unloaded speed of shortening, $v_u(t)$, and fiber acceleration, $a_u(t)$

With the line-scan recording, the time course of shortening can be reliably measured at a 10-fold faster time resolution compared to the video acquisition (half-frames). The advantage of this increased resolution can be impressively demonstrated by the evaluation of the maximum unloaded speed of shortening, $v_{u,max}$, and acceleration, $a_{u,max}$. Fig. 5 *A* shows the whole time course of $v_u(t)$ in another single BALB/C interossei fiber at

TABLE 1 Temperature dependence of the onset latency, l_{min}/L_0, TTM, $v_{u,max}$, and TT $v_{u,max}$ recorded at 500 Hz in single BALB/c (and C57 wt at 24°C) interossei fibers

Temperature (°C)	Onset latency (ms)	l_{min}/L_0	TTM (ms)	$v_{u,max}$ (L_0 s^{-1})	TT$v_{u,max}$ (ms)	n
10	30.5 ± 6.1	0.67 ± 0.06	923 ± 78	5.75 ± 0.99	51.0 ± 9.3	4
20	19.0 ± 0.6	0.52 ± 0.03	832 ± 37	13.25 ± 2.02	28.5 ± 7.4	4
24	23.5 ± 1.2	0.57 ± 0.04	506 ± 77	12.54 ± 2.54	41.3 ± 3.6	11
30	19.5 ± 1.7	0.55 ± 0.02	395 ± 23	13.94 ± 1.37	35.0 ± 7.0	4

TABLE 2 Temperature dependence of peak I_{Ca}, TTP during maintained depolarizations, and $[Ca^{2+}]_i$ (I_{Ca}) at the TT$v_{u,max}$ and at the end of the 1-s lasting pulse in single BALB/c interossei fibers

Temperature (°C)	Peak I_{Ca} (μA/cm^2)	TTP (ms)	$[Ca^{2+}]_i$ (I_{Ca}) at TT$v_{u,max}$ (μM)	$[Ca^{2+}]_i$ (I_{Ca}) at 1 s (μM)	n
10	−31.47 ± 5.90	185 ± 64	2.76 ± 1.18	75.6 ± 17.9	4
20	−31.68 ± 7.12	76 ± 9	1.70 ± 0.76	58.9 ± 13.8	4
24	−54.51 ± 3.20	53 ± 8	6.55 ± 1.74	72.5 ± 20.0	4
30	−51.81 ± 0.93	19 ± 3	11.87 ± 3.66	61.4 ± 16.1	4

30°C with its corresponding $l(t)$ recording, as shown in the upper inset. The more interesting initial 50 ms are shown on an extended timescale along with the corresponding I_{Ca} trace and the I_{ca}-induced $[Ca^{2+}]_i$ rise in the lower two insets. The maximum speed of shortening, $v_{u,max}$, was close to 16 fiber lengths/s (L_0 s^{-1}) in this recording. In several fibers at four different temperatures, $v_{u,max}$ measured 5.7 ± 1.0 (10°C, n = 4), 13.2 ± 2.0 (20°C, n = 4), 12.5 ± 2.5 (24°C, n = 11), and 14.0 ± 1.4 (30°C, n = 4) L_0 s^{-1} (Fig. 5 *B*). Note that values from both BALB/c and C57 wt mice were not significantly different ($P = 0.27$), and are lumped together here (~24°C). In those experiments where simultaneous video recordings were available, $v_{u,max}$ was also calculated from the image sequences. Those values were substantially smaller than those obtained from the 10-times-faster line-scan recordings (Fig. 5 *B*, *black hatched bars*). To test whether the video image resolution (50 Hz) could be predicted from the 500-Hz line-scan recording, a 50-Hz low-pass filter was applied to the line-scan data. The corresponding data are shown as hatched bars in Fig. 5 *B* (50 Hz average). As can be clearly seen, the video data are well reproduced from the filtering procedure of $l(t)$. Those data underestimate $v_{u,max}$ from the 500-Hz line-scan recordings by ~65%.

In the previous section, it was suggested that shortening occurs at saturating myoplasmic Ca^{2+} concentrations sufficient

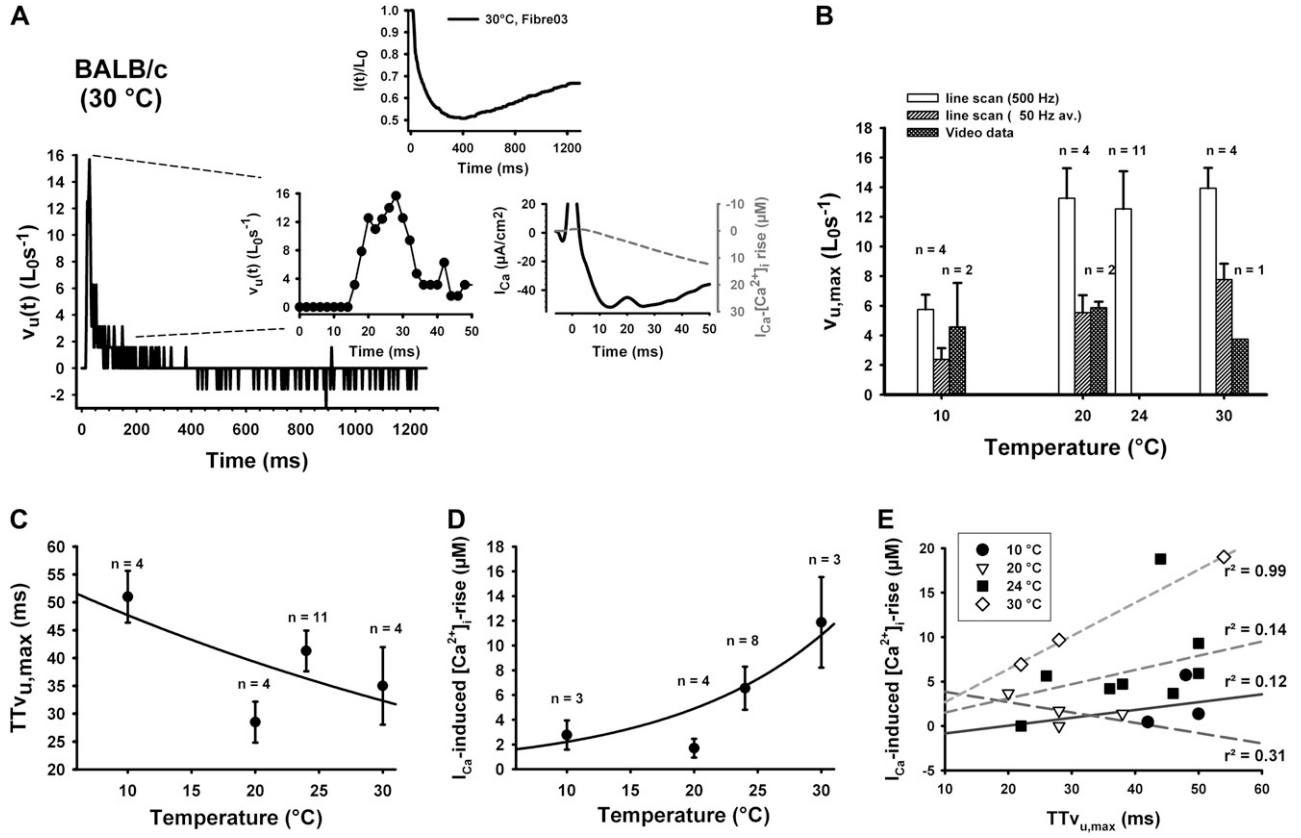

FIGURE 5 Unloaded speed of shortening $v_u(t)$ recorded at 500 Hz and compared to 50-Hz video data in single interossei fibers. (*A*) Time course of $v_u(t)$ in a single adult BALB/c fiber at 30°C derived from $l(t)$ recorded with the line scan at 500 Hz, as shown in the upper inset for this fiber. Data are given as relative fiber lengths, $l(t)/L_0$. $v_u(t)$ already has its maximum, $v_{u,max}$, of ~16 L_0 s^{-1} after 28 ms. The two lower insets show $v_u(t)$ on an extended timescale for the first 50 ms, as well as the simultaneously recorded I_{Ca} trace and the calculated I_{Ca}-induced rise in $[Ca^{2+}]_i$ for this fiber. Note that the hump in the I_{ca} trace at 20 ms is an artifact. (*B*) Statistics for $v_{u,max}$ in several fibers for the temperatures indicated (*white bars*). Results from BALB/c and C57 wt interossei fibers available at ~24°C were not significantly different and are lumped together here. In some experiments, simultaneous video sequences (recorded at 50 Hz) were also available, from which $v_{u,max}$ was also calculated (*dark-hatched bars*). When applying a 50-Hz low-pass filter to the line-scan data, $v_{u,max}$ from the video sequences was accurately predicted (*diagonally hatched bars*, 50 Hz average). $v_{u,max}$ was significantly larger for temperatures of 20°C and above compared to 10°C ($P < 0.001$). Temperature dependence of TT$v_{u,max}$ (*C*), calculated I_{Ca}-induced rise in $[Ca^{2+}]_i$ at TT$v_{u,max}$ (*D*), and correlation of both parameters at the different temperatures (*E*) show weak linear correlations for lower temperatures but a strong linear correlation for larger temperatures. See text for details.

to give maximum force when one calculates the I_{Ca}-induced rise in $[Ca^{2+}]_i$ by the end of the pulse (Table 2). However, this might be less clear if the time soon after the depolarization (when shortening velocity reaches its maximum) is regarded. This time to $v_{u,max}$ ($TTv_{u,max}$) was evaluated and its temperature dependence is shown in Fig. 5 *C*. With increasing temperature, $TTv_{u,max}$ decreased, and an exponential fit was drawn through the data (*solid line*). The corresponding I_{Ca}-induced $[Ca^{2+}]_i$ rise at this time point of maximum unloaded shortening was then calculated and its temperature dependence is shown in Fig. 5 *D* with an exponential fit to the data. Note that at 24°C, I_{Ca} traces in three fibers were distorted during the shortening phase and excluded from the analysis. The data show that at $TTv_{u,max}$, the I_{Ca}-induced rise in $[Ca^{2+}]_i$ was at least 5 μM for temperatures >20°C, which is due mainly to the faster activation of I_{Ca} at these temperatures (Table 2). Therefore, maximum initial shortening can be assumed to occur at saturating myoplasmic Ca^{2+} concentrations, at least for larger temperatures. Fig. 5 *E* finally shows the correlations between $TTv_{u,max}$ and I_{Ca}-induced rise in $[Ca^{2+}]_i$ at $TTv_{u,max}$ for the different temperatures in all individual fibers from which both data sets were available. A linear correlation was most pronounced for larger temperatures. At lower temperatures, the I_{Ca}-induced rise in $[Ca^{2+}]_i$ was very small and eventually even zero in the 10°C case, simply because TTP of I_{Ca} greatly exceeded $TTv_{u,max}$ (Table 2).

Fig. 6 *A* shows the time course of the complete unloaded acceleration transient, $a_u(t)$, of the fiber shown in Fig. 4 *A*. The corresponding $v_u(t)$ is shown in the upper inset. The more interesting initial phase of $a_u(t)$ is again shown on an extended timescale in the lower inset along with the corresponding I_{Ca} and I_{Ca}-induced $[Ca^{2+}]_i$-rise transients. Also shown in the $a_u(t)$ panel is the 50-Hz filtered version of the data (*gray line*). It is obvious that the very fast maximum of fiber acceleration is substantially underestimated by a 10-times-slower recording that could not be adequately analyzed from the video data due to the lack of data points in the first 50 ms of shortening (two points only in the video data). Between 10°C and 20°C, $a_{u,max}$ almost doubled and remained relatively stable around ~3000 L_0 s^{-2} for higher temperatures (Fig. 6 *B*).

Shortening kinetics in single fibers from adult wt, mdx, and MinD mice

This section deals with the application of the high-speed shortening acquisition to single fibers related to the pathophysiology of Duchenne muscular dystrophy. Examples of representative $l(t)$ traces in single fibers from wt, mdx, and MinD mice at 25°C were shown in Fig. 4 *B*. Fig. 7 shows the analysis from several recordings of $l(t)$ in these strains at both 15°C and 25°C. Similar to the BALB/c strain, the degree of shortening was more complete and accelerated at the higher temperature, as reflected by a decrease in l_{min}/L_0 (Fig. 7 *A*), TTM (Fig. 7 *B*), τ_1 (Fig. 7 *C*), and τ_2 (Fig. 7 *D*). In mdx fibers, compared to wt fibers, TTM and time constants of shortening seemed to be consistently larger, but only significantly so for τ_1 and τ_2 at 15°C. Although this suggests a somewhat slower unloaded shortening kinetics, the maximum degree of shortening was larger in these fibers compared to controls at 25°C (l_{min}/L_0~43% vs. ~50%). At 15°C, however, it seems there was no difference in minimum fiber length, although there was an even more pronounced prolongation of kinetics. $v_{u,max}$ was very similar in all strains, measuring ~9 L_0 s^{-1} at 15°C and ~15 L_0 s^{-1} at 25°C (Fig.

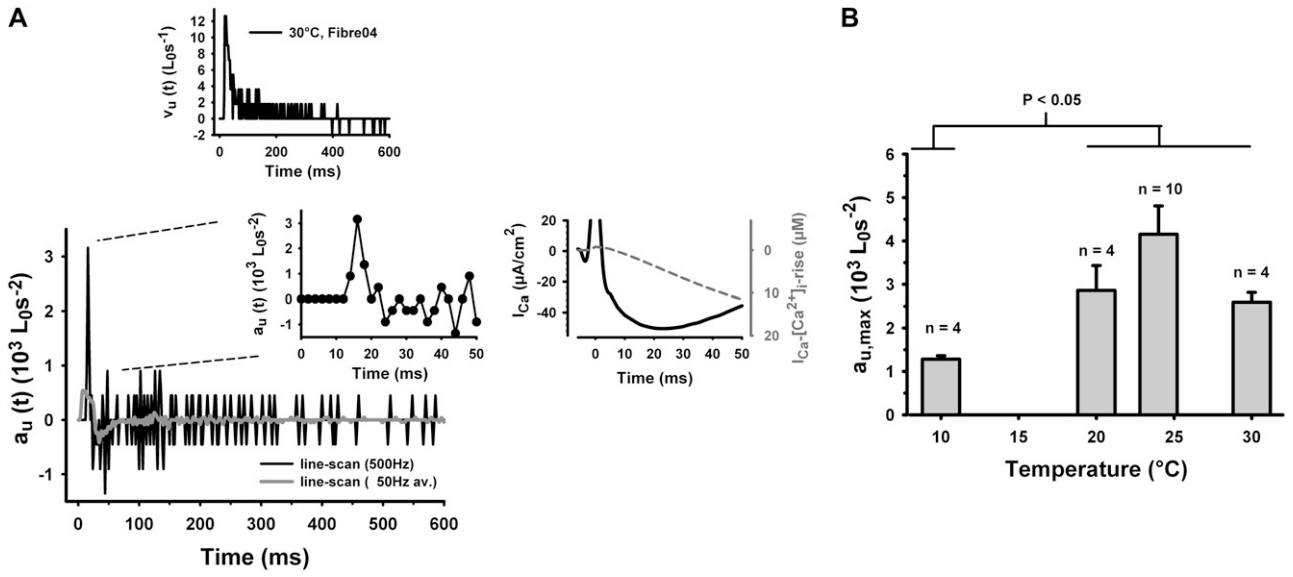

FIGURE 6 Unloaded shortening acceleration, $a_u(t)$, recorded at 500 Hz in single interossei fibers. (*A*) Time course of $a_u(t)$ in the single fiber shown in Fig. 4 *A* at 30°C. Also shown is the 50-Hz filtered version of the signal (*gray line*) that markedly reduces maximum amplitude. In this fiber, $a_{u,max}$ is ~3000 L_0 s^{-2} at 16 ms, followed by a quick deceleration to −1350 L_0 s^{-2} at ~40 ms. (*B*) Statistics of $a_{u,max}$ from a number of fibers. Note that due to the very coarse time resolution, $a_{u,max}$ could not accurately be obtained from video sequences.

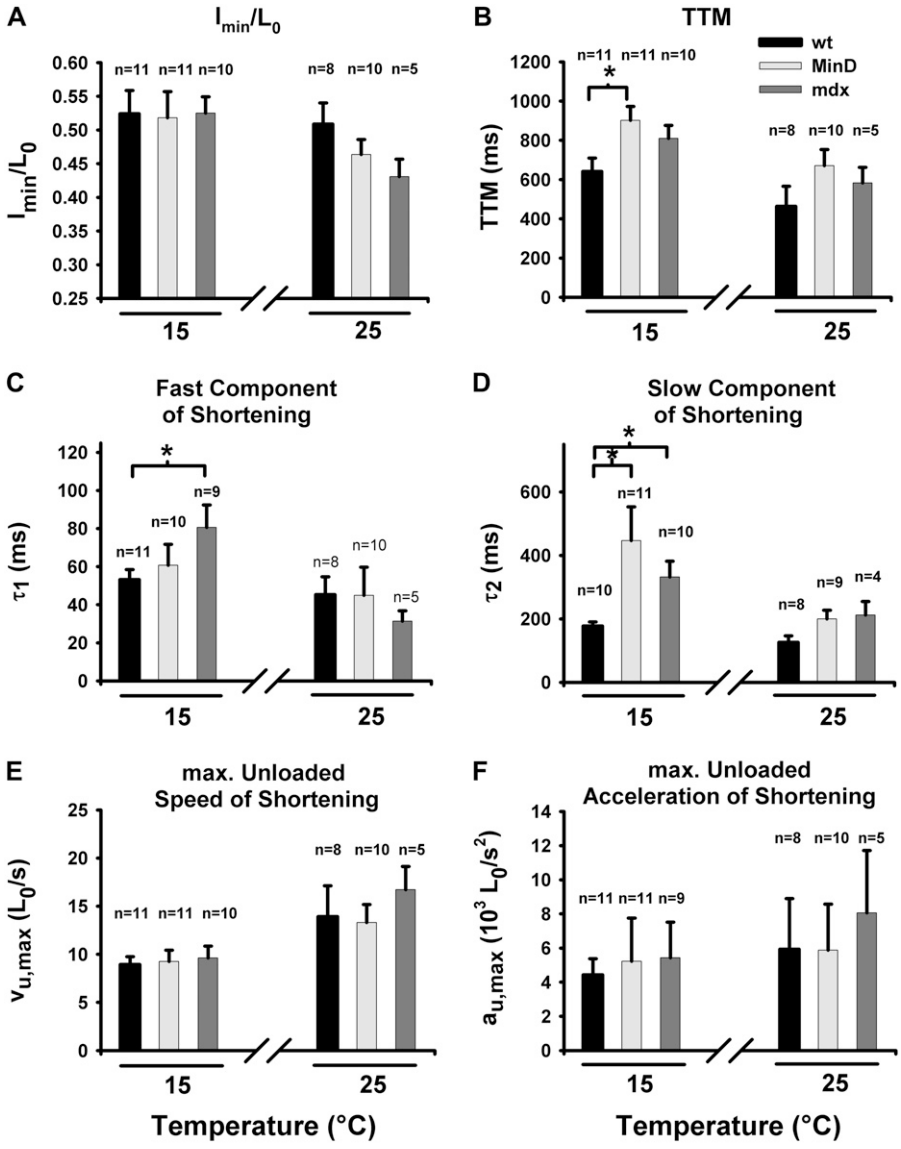

FIGURE 7 Unloaded shortening kinetics and parameters from line-scan recordings at 500 Hz in single adult wt, mdx, and MinD fibers. Unloaded shortening was recorded with the 500-Hz line-scan technique in several (n) single fibers from adult wt, mdx, and MinD mice of similar age (see Fig. 4 for age bins) at 15°C and 25°C. (A–F) l_{min}/L_0, TTM, τ_1, τ_2, $v_{u,max}$, and $a_{u,max}$ are shown. Some n values in the figure are smaller, either due to outlier detection and removal or to $l(t)$ traces being somewhat distorted, and these could not be reliably fitted (particularly for τ_1 or τ_2). For details, see text. $^*P < 0.05$.

7 E). Similarly, there was no statistically significant difference between the genotypes for $a_{u,max}$ at either temperature ($P > 0.44$ at 15°C, $P > 0.19$ at 25°C, Fig. 7 F). Note that the number of observations was smaller for some parameters either after elimination of an outlier or due to fitting failure in cases where $l(t)$ traces were distorted.

Analysis of MHC and MLC protein contents in interossei muscle fiber bundles from wt, mdx, and MinD mice

To validate our robust findings of unaltered $v_{u,max}$ in wt, mdx, and MinD fibers, we performed SDS-PAGE analysis of MHC and MLC protein contents in interossei muscles of the three genotypes. Fig. 8 A shows representative gels to separate MHC isoforms from muscle extracts of soleus, EDL, and interossei C57 wt muscle. The MHC protein bands in soleus and EDL muscle are typically referred to as MHC I, MHC IIA, MHC IIB, and MHC IIX, according to their molecular weight from literature data, and using MHC standards (50,54,55). Soleus muscle shows the typical predominance of MHC I and MHC IIA, whereas in EDL muscle MHC IIX and MHC IIB distributions prevail. Interossei muscle homogenates show a single band reflecting MHC IIA for all three genotypes. This is also demonstrated in the protein density profile of the lanes that shows perfect matching of the curves with the MHC IIA peak from soleus muscle (Fig. 8 B). Fig. 8 C shows corresponding SDS gels for the MLC distributions. In mdx interossei muscles, some reduction in the MLC-2f and MLC-3f protein bands might be anticipated compared to both wt and MinD muscles, which is also suggested from the protein density profile (Fig. 8 D). This trend could be confirmed when evaluating the relative protein contents of the fast MLC isoforms from up to nine gels of the three genotypes (Fig. 8 E). However, the decrease

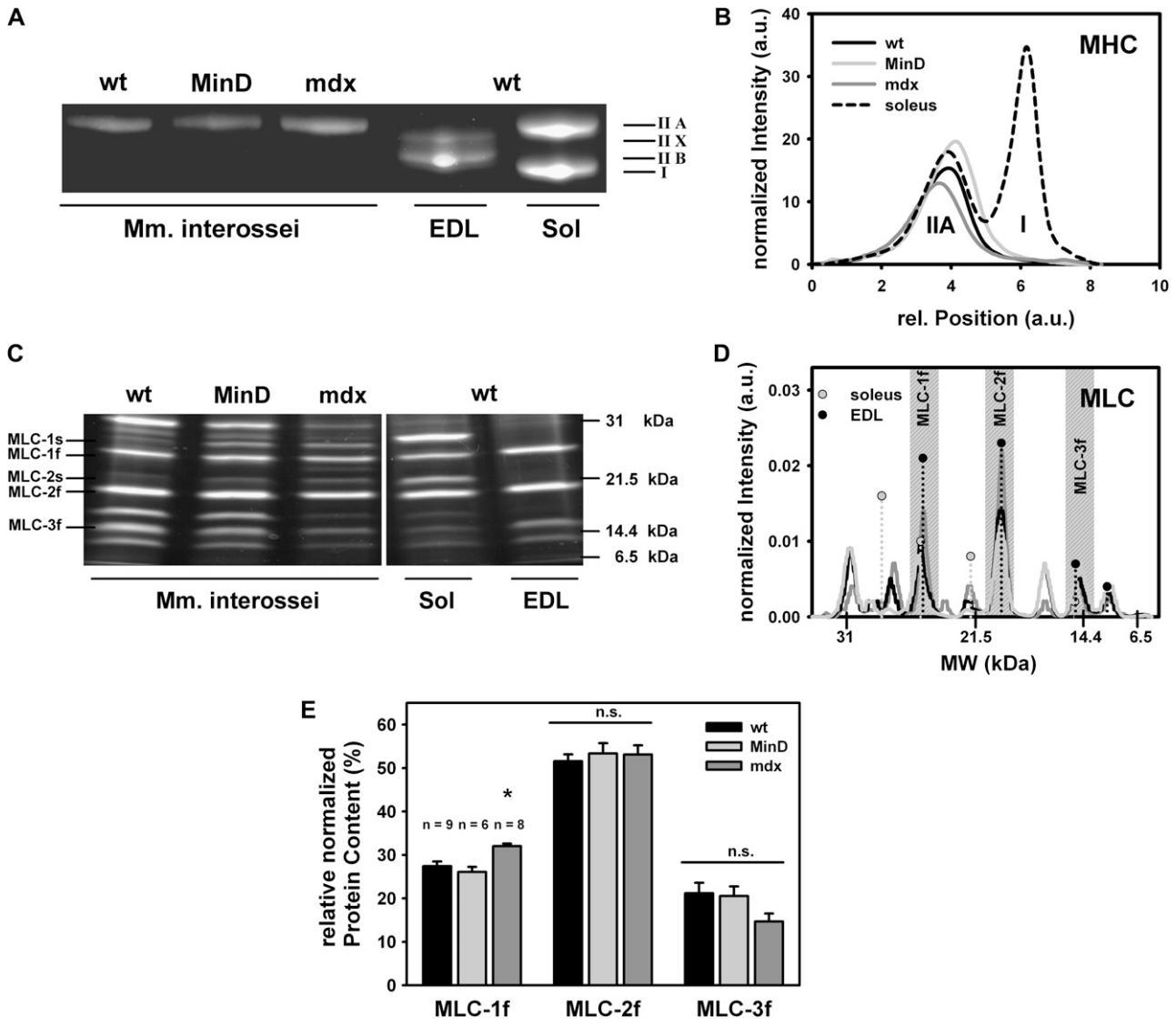

FIGURE 8 SDS-PAGE analysis of MHC and MLC protein contents in interossei muscle fiber bundles from wt, mdx, and MinD mice. (*A*) Representative 8% SDS-PAGE gels from wt, MinD, and mdx interossei muscle homogenates to separate MHC. The corresponding gels from wt EDL and soleus muscle are shown in the right two lanes for comparison. Soleus and EDL muscles show the well-known MHC isoform distributions of IIA and I and IIX and IIB, respectively. There is no difference in the protein distributions from the three strains in interossei muscles, as confirmed by the densitometry (*B*). The single bands in those gels solely represent MHC-IIA, as confirmed by comparison with the bands from soleus muscle. (*C*) MLC profiles of 12% SDS-PAGE gels from the three genotypes and muscles shown in *A*. The fainter staining of the ~16.5-kDa band in mdx interossei muscle, corresponding to MLC-3f, compared to wt and MinD interossei muscles, is also seen in the densitogram (*D*). The corresponding peaks from wt EDL and soleus muscles are shown as vertical dotted lines in *D*. (*E*) The somewhat reduced MLC-3f content is confirmed in the relative contents of fast MLC isoforms from several gels but is, however, not statistically significant. MLC-1f content is significantly larger in mdx muscle (*: $P < 0.01$).

in mdx MLC-2f and MLC-3f did not reach statistical significance ($P > 0.07$). In addition, a statistically significant increase in the mdx MLC-1f content was seen ($P < 0.01$).

DISCUSSION

L-type Ca^{2+} currents during unloaded shortening in single interossei fibers

In this work, we have introduced a what to our knowledge is a new technique to directly monitor unloaded shortening in intact isolated mammalian skeletal interossei muscle fibers that allows simultaneous recordings of L-type Ca^{2+} currents. Using this line-scan technique, the full time course of fiber length, velocity, and acceleration was monitored at a sampling rate of 500 Hz and time-correlated to the electrophysiological data. Maximum peak I_{Ca} values showed bimodal temperature dependence with similar values for 10°C and 20°C and about two-times-larger values between 20°C and 30°C. Similar Q_{10} values of 2–2.5 for an increase in I_{Ca} have been described in rat omohyoid (56) and human vastus la-

teralis muscle (57). Likewise, in the same studies, TTP, or rise time, as a measure for channel activation, decreased 2.5- to 3-fold. Under single-twitch conditions, where L-type Ca^{2+} channels mainly act as voltage sensors and not as conducting channels (53), myoplasmic $[Ca^{2+}]_i$ rises primarily due to fast SR Ca^{2+} release. Using proper Ca^{2+} sensitive dyes, peak $[Ca^{2+}]_i$ in single mouse EDL fibers during single twitches reached ~22 μM within ~2 ms at 28°C (52). In rat EDL fibers, the peak of the Ca^{2+} transient of ~4.5 μM was reached after ~4.5 ms in response to single action potentials (51). In skinned rat EDL fibers, maximum force occurred from myoplasmic $[Ca^{2+}]$ values of ~7–10 μM at 35°C and force-Ca^{2+} relationships were shifted toward larger pCa values (i.e., lower myoplasmic $[Ca^{2+}]_i$) with decreasing temperature (58). Under our conditions of maintained depolarizations in voltage-clamped single interossei fibers, intracellular $[Ca^{2+}]$ is expected to remain at levels that fulfill maximum activation of the contractile apparatus for the whole recording period. The early phase of transient SR Ca^{2+} release that we cannot resolve with our electrophysiology technique is followed by I_{Ca} influx through the L-type channel that in turn results in an additional I_{Ca}-induced rise in $[Ca^{2+}]_i$. By the end of the pulse, this I_{Ca}-induced rise in $[Ca^{2+}]_i$ obviously exceeds the ~20 μM myoplasmic $[Ca^{2+}]_i$ from SR release ~3-fold. I_{Ca}-induced $[Ca^{2+}]_i$ rise was temperature-dependent and linearly correlated with the time of maximum unloaded speed of shortening $TTv_{u,max}$ for larger temperatures (i.e., 30°C, Fig. 5 *E*). For lower temperatures, I_{Ca}-induced $[Ca^{2+}]_i$ rise was still small at $TTv_{u,max}$ (<7 μM (Fig. 5 *D*)), but $v_{u,max}$ values themselves were quite similar between 20°C and 30°C (see below). Therefore, it seems that the first phase of shortening is not limited by the I_{Ca}-induced $[Ca^{2+}]_i$ rise but rather by the SR-induced $[Ca^{2+}]_i$ rise and myofilament-based mechanisms.

Temperature dependence of unloaded shortening kinetics in normal interossei fibers

During depolarization-induced shortening, fibers contracted to ~55% of the initial resting length, L_0. l_{min}/L_0 was similar for temperatures from 20°C and somewhat larger for lower temperatures (~65% at 10°C). $l(t)$ showed a characteristic biexponential activation phase. The biexponential shortening of the whole fiber upon maintained depolarizations is also reflected on the sarcomere level. Recent results from video tracking of Ca^{2+}-activated rabbit psoas myofibrils consisting of 10–20 individual sarcomeres also showed a biphasic shortening kinetics of half-sarcomere lengths upon Ca^{2+} activation at pCa of 4.5 (59). The time constants of half-sarcomere shortening were in the second range which can be explained by differences in muscle type used (slow in Telley et al (59) versus fast in this study), but more obviously by technical differences (solution-exchange-induced Ca^{2+} activation of isolated myofibrils versus intracellular depolarization of intact fibers in this study). The question arises, what are the underlying mechanisms reflected by the two exponentials during unloaded shortening? Telley et al. (59) did not further comment on their biexponential shortening on the sarcomere level, but from their and other studies, it seems clear that active shortening is not an instantaneous consequence of force during force development. Current cross-bridge models also propose that force-generating steps precede the step determining active shortening velocity (59). We postulate that shortening processes represented by both the fast- and slow-activation kinetics under our conditions might be related to an initial fast shortening phase that is entirely unloaded and related to the near-optimal overlap of the filaments at the start of contraction (sarcomere lengths ~2.2–2.4 μm, O. Friedrich, unpublished observation), followed by a slower phase that contains shortening against an increasing ''internal load'' that might arise from interference with and bending of the filaments as the fiber shortens to less than two-thirds of its original length in most of our fibers. Series elastic elements and noncycling cross-bridges would also oppose shortening with decreasing sarcomere lengths. The importance of an ''instantaneous elasticity element'' with a velocity-dependent behavior has been emphasized by Podolsky and Nolan (60). It is also interesting to note that in most studies on mammalian muscle fibers, the tension decline during ramp shortening occurs in two phases (e.g., (61)). Whether this relates to the biexponential shortening phases during unloaded shortening is currently not known and would be an important question for future studies.

The temperature dependence of the time constants for the two shortening phases in normal fibers was used to calculate the activation energies, E_a (Fig. 4 *D*). To our knowledge, activation energies for the complete time course of unloaded shortening have not yet been given. With 59 kJ/mol for τ_1 and 47 kJ/mol for τ_2, our values are quite similar to activation energies for other shortening parameters that were calculated for mammalian muscle. For example, in intact rat EDL and soleus muscle fibers contracting isotonically after release from an isometric tetanus-induced contraction, E_a of $v_{u,max}$ derived from force-velocity relations were in the range of 40–45 kJ/mol for both muscles (62). For rates of tension development, E_a values were 48 kJ/mol for EDL and 56 kJ/mol for soleus muscle, respectively (62). This is a further indication that the second slower phase in our shortening fibers may be affected by build-up of retracting force in the tens of milliseconds range (see Fig. 3 in (62)).

Maximum unloaded speed of shortening and acceleration in normal interossei fibers

With this acquisition technique, calculated $v_{u,max}$ values were substantially larger compared to values derived from video acquisition experiments, as expected from the much lower time resolution of the latter (Fig. 5 *B*). This was, for example, correctly predicted from experiments where both video and CCD recordings were performed and the latter additionally

subjected to a 50-Hz filter (simulates half-frame resolution at 20-ms repetition rate (Fig. 5 *B*)). As in previous studies using mammalian muscle fibers, $v_{u,max}$ was temperature-dependent (e.g., (25,63)). Between 10°C and 20°C, the Q_{10} value for $v_{u,max}$ was 2.3, whereas between 20°C and 30°C, Q_{10} values were close to unity. This parallels findings from rat EDL muscle fibers, where a much greater temperature dependence of $v_{u,max}$ was found below 25°C as compared to above 25°C (63). Nyitrai et al. (55) give a possible explanation from their cross-bridge dissociation experiments using ATP-induced acto-heavy-meromyosin dissociation (55). For mammalian fast skeletal muscles, the rate constant of ADP release that limits cross-bridge detachment and contraction velocity becomes rate-limiting for velocity above temperatures of ~25°C, but only with a very small temperature dependence (55). Interestingly, when comparing our $v_{u,max}$ values to data from force-velocity and slack-test experiments in the literature, our direct observation of unloaded shortening suggests larger values than previously described. Some examples for $v_{u,max}$ values from force-velocity relations include: $\sim 4\ L_0\ s^{-1}$ at 21–27°C in mouse flexor digitorum brevis fibers (64), 6–10 $L_0\ s^{-1}$ at 30°C in rat EDL (62,63), $\sim 9\ L_0\ s^{-1}$ at 26°C in mouse diaphragm (41), $\sim 6\ L_0\ s^{-1}$ at 21°C in mouse EDL fibers (65), or $\sim 1\ L_0\ s^{-1}$ at 12°C in human vastus lateralis (IIA, IIB) muscle fibers (66). On the other hand, $v_{u,max}$ values of ~30–60 $L_0\ s^{-1}$ have been found in ultrafast rabbit inferior oblique muscles for temperatures between 20°C and 35°C (67). Two examples of $v_{u,max}$ values obtained from slack tests are $\sim 12.5\ L_0\ s^{-1}$ at 32°C in mouse flexor digitorum brevis fibers (25) or $\sim 3\ L_0\ s^{-1}$ at 12°C in rat fast muscle fibers (12). Up to 30% larger values for $v_{u,max}$ obtained from slack-test experiments have been described compared to force-velocity relationships in intact and even up to 50% in skinned fibers (24). Basically, three explanations have been suggested for this phenomenon (20): 1), the slack test method suffers from inaccuracy in determining the exact time interval for taking up the slack; 2), the Hill curve deviates from the recorded force-velocity relation in the range of very low and very high loads, thus underestimating $v_{u,max}$; and 3), there is a discontinuity in the force-velocity relation for truly unloaded conditions. The authors (20) have already pointed out the necessity to directly image fiber length during shortening to better correlate the different techniques. That has been successfully addressed by means of the one-dimensional recording array in this study. It seems that $v_{u,max}$ values from fast recordings of unloaded shortening in intact mammalian toe muscle fibers under voltage-clamp conditions indeed exceed $v_{u,max}$ values from slack-test recordings by an additional 40–50%.

Apart from myosin ATPase activity and myoplasmic Ca^{2+} concentrations, the main determinants of $v_{u,max}$ are given by the MHC and MLC distributions, which may differ substantially in different muscles and even in the same muscle under different physiological or pathophysiological conditions (12,16,55). To date, MHC and MLC distributions in mammalian interossei muscles have been very poorly described and, to the best of our knowledge, not at all in mouse. In our murine interossei muscle preparations, SDS PAGE analysis showed a single MHC IIA band. The corresponding MLC protein distribution (Fig. 8 *B*, *wt*) showed a very similar pattern compared to a variety of other mammalian fibers investigated (55). Therefore, we think that the larger $v_{u,max}$ values under our conditions are not a result of a different MHC/MLC fiber composition but rather reflect a high maximum shortening velocity during a very short time interval in the initial shortening phase, which may have been undetected from both slack tests and force-velocity relations due to the time resolution and other constraints mentioned above. A further advantage of our technique is that the acceleration of unloaded shortening can be directly obtained. Depending on temperature, $a_{u,max}$ values of several thousand fiber lengths/s^2 were obtained.

Unloaded shortening characteristics of voltage-clamped interossei fibers from wt, mdx, and MinD mice

Several studies have found altered contractile properties associated with the lack of dystrophin in mdx mice, although the exact molecular mechanisms remain elusive (36). For example, specific twitch and peak isometric tetanic force are consistently lower in mdx versus wt mice >5 months old, whereas absolute force values can be normal by reactive muscle hypertrophy for a long time during the lifespan of the mdx animal (40). Fatigue resistance in some mdx limb muscles and the diaphragm was found to be either at control levels or even increased, probably due to MHC fast-to-slow conversions with greater oxidative capacity (68). The shortening dynamics of mdx muscle has been addressed in a few studies only (summarized, e.g., in (36)). Force-velocity relations were downward-shifted in EDL mdx muscle (40). These findings were compatible with MHC shifts from fast to slow isoforms and reduced amounts of MLC-3f (16,69). In mdx diaphragm, impaired dynamics of shortening was explained by prolonged cross-bridge cycle durations and slower cross-bridge detachment rates, based on calculations from Huxley's equations (41). In our interosseus muscle preparation, we confirmed the changes seen in MLC isoform distributions in EDL muscle, with a tendency toward reduced MLC-3f and MLC-2f isoforms (Fig. 8 *E*). In addition, we found a significant increase in MLC-1f levels. In contrast to EDL muscle (16), MHC distributions were identical in wt, mdx, and MinD interossei muscles (Fig. 8 *A*). This may be also reflected in our $v_{u,max}$ values. At two temperatures (15°C and 25°C), $v_{u,max}$ and $a_{u,max}$ were similar in mdx versus wt or MinD fibers (Fig. 7, *E* and *F*). There was a significant prolongation of both shortening time constants in mdx fibers, but only at 15°C, whereas for temperatures that are more physiological in toe muscles (~25–30°C), our data suggest no differences in unloaded shortening kinetics per se. This is in agreement with recent findings in maturing EDL muscle from

mdx mice, where no difference in passive mechanical and viscoelastic properties was found before or after the overt onset of the dystrophic process (14–35 days) (70). Nevertheless, the observed differences in shortening parameters may be, at least partly, also related to differences in the phosphorylation of MLC that are known to modulate shortening velocities (17). Further research will help to clarify whether there are substantial differences in MLC phosphorylation between these genotypes.

In summary, we have presented what to our knowledge is a new imaging technique that allows high-speed recording of unloaded shortening in single intact voltage-clamped muscle fibers. Maximum unloaded speed of shortening was faster than recorded with other, more indirect, methods. From our results, it is likely that the contractile kinetics contributing to initial unloaded shortening, i.e., weak binding states and detachment rates, are not affected in our animal model of DMD. It will be interesting to apply our technique to other classical fiber models that differ in MHC isoform composition (e.g., soleus and psoas muscle) to clarify which of the parameters depend on MHC isoform. For other pathophysiological conditions in muscle that might be associated with altered cross-bridge kinetics, e.g., critical illness myopathies, we think our technique will provide a valuable tool to elucidate some of the underlying pathological mechanisms.

APPENDIX: ERROR ESTIMATE OF SHORTENING DUE TO FIBER GEOMETRY

This section deals with the estimate of the error that could be introduced to $v_{u,max}$ with the line-scan technique when bending is present in single fibers. Fig. 3 shows an image of a bent single fiber and the relative position of the CCD line through the fiber middle. The latter will only trace the time course of the fiber ending projections on the CCD line. From the initial image, the fiber contour is described by an arc segment $b = l_{opt.}(t)$ with radius $r(t)$ and angle $\alpha(t)$. The actual position of the CCD line is in parallel to the secant of the arc segment, $a = l_{CCD}(t)$ and linearly shifted into the fiber middle to cover most of the fiber length. a represents the actual fiber length $l(t)$ recorded by the CCD line ($l_{CCD}(t)$). The angle $\alpha(t = 0)$ was determined from the initial image to $\sim\pi/4$. This was also the maximum allowed initial angle for the use of bended fibers (see below). An estimate of the initial ratio a_0/b_0, i.e., at $t = 0$, yields the maximum error in fiber-length recordings using, for the radius, $r(t)$, and the secant of the arc, the relations

$$r(t) = \frac{b(t)}{\alpha(t)} \approx \left.\frac{4b_0}{\pi}\right|_{t=0,\alpha=\frac{\pi}{4}}; \tag{A1}$$

$$\alpha = 2r(t) \times \sin\frac{\alpha(t)}{2} \approx \left.\frac{8}{\pi}b_0 \times \sin\frac{\pi}{8}\right|_{t=0,\alpha=\frac{\pi}{4}}. \tag{A2}$$

With the expansion series $\sin(\pi/8) \approx (\pi/8) - (1/3!(\pi/8)^3)$, it follows that

$$a_0 \approx b_0\left(1 - \frac{\pi^2}{1728}\right) = 0.9421 \times b_0. \tag{A3}$$

The maximum deviation of the projected initial fiber length on the CCD line from the apparent fiber length is supposed to be <6% for maximum curvatures of $\pi/4$. This error is expected to quickly decrease within the first tens of milliseconds of shortening, because fibers are fixed by the microelectrodes in their centre of mass, and therefore the curvature will rapidly decrease during shortening as the fiber endings move along the arc to the fiber middle (Fig 3, *black arrows*). The fiber endings, therefore, initially perform a translational as well as a small rotational trajectory. The CCD line, however, keeps tracking the projected fiber lengths, i.e. a translational movement (Fig. 3, *gray arrows*) that is smaller than the apparent distance covered by the fiber endings during the same time interval. From a time $\hat{t}$, shortening will be almost completely translational for all $t > \hat{t}$, as $r \to \infty \ \wedge \ a \to 0$:

$$\begin{aligned} a = l_{CCD}(t > \hat{t}) &\approx \frac{2b}{\alpha}\left(\frac{\alpha}{2} - \frac{\alpha^3}{3! \times 2^3} \pm \ldots\right) \\ &\approx b\left(1 - \frac{\alpha^2}{108}\right) = \left. l_{opt.}(t)\right|_{\alpha \to 0}. \end{aligned} \tag{A4}$$

From video images, fiber bending was already completely absent after two to three successive images, i.e., 20–40 ms. It may be that bending is already removed earlier but cannot be detected due to the too-slow video acquisition. As $v_{u,max}$ is reached in a time interval that lies within the window where $h(t) \to 0$ ($h(t) > 0$), the shortening velocity recorded by the CCD line still somewhat underestimates the apparent fiber shortening velocity because the projected fiber endings cover smaller distances during the sampling intervals than do the still bent fiber endings (see above). Therefore, our $v_{u,max}$ values given in Results may represent a lower limit for unloaded shortening velocities in voltage-clamped single fibers.

REFERENCES

1. Stephenson, D. G. 2006. Tubular system excitability: an essential component of excitation-contraction coupling in fast-twitch fibers of vertebrate skeletal muscle. *J. Muscle Res. Cell Motil.* 27:259–274.
2. Lamb, G. D. 2002. Voltage-sensor control of Ca^{2+}-release in skeletal muscle: insights from skinned fibers. *Front. Biosci.* 7:d834–d843.
3. Berchtold, M. W., H. Brinkmeier, and M. Müntener. 2000. Calcium ion in skeletal muscle: its crucial role for muscle function, plasticity, and disease. *Physiol. Rev.* 80:1215–1265.
4. Galler, S., B. G. Wang, and M. Kawai. 2005. Elementary steps of the cross-bridge cycle in fast-twitch fiber types from rabbit skeletal muscles. *Biophys. J.* 89:3248–3260.
5. Huxley, A. F. 2000. Mechanics and models of the myosin motor. *Philos. Trans. R. Soc. Lond. B Biol. Sci.* 355:433–440.
6. Gordon, A. M., E. Homsher, and M. Regnier. 2000. Regulation of contraction in striated muscle. *Physiol. Rev.* 80:853–924.
7. Lieber, R. L., and S. C. Bodine-Fowler. 1993. Skeletal muscle mechanics: implications for rehabilitation. *Phys. Ther.* 73:844–856.
8. Hooft, A. M., E. J. Maki, K. K. Cox, and J. E. Baker. 2007. An accelerated state of myosin-based actin motility. *Biochemistry.* 46:3513–3520.
9. Hook, P., and L. Larsson. 2000. Actomyosin interaction in a novel single muscle fiber in vitro motility assay. *J. Muscle Res. Cell Motil.* 21:357–365.
10. Stehle, R., and B. Brenner. 2000. Cross-bridge attachment during high-speed active shortening of skinned fibers of the rabbit psoas muscle: implications for cross-bridge action during maximum velocity of filament sliding. *Biophys. J.* 78:1458–1473.
11. Toniolo, L., L. Maccatrozzo, M. Patruno, E. Pavan, F. Caliaro, R. Rossi, C. Rinaldi, M. Canepari, C. Reggiani, and F. Mascarello. 2007. Fiber types in canine muscles: myosin isoform expression and functional characterization. *Am. J. Physiol. Cell Physiol.* 292:C1915–C1926.
12. Bottinelli, R., R. Betto, S. Schiaffino, and C. Reggiani. 1994. Unloaded shortening velocity and myosin heavy chain and alkali light chain isoform composition in rat skeletal muscle fibres. *J. Physiol.* 478:341–349.
13. Reiser, P. J., R. L. Moss, G. G. Giulian, and M. L. Greaser. 1985. Shortening velocity in single fibers from adult rabbit soleus muscles is

correlated with myosin heavy chain composition. *J. Biol. Chem.* 260: 9077–9080.

14. Andersen, J. L. 2003. Muscle fiber type adaptation in the elderly human muscle. *Scand. J. Med. Sci. Sports.* 13:40–47.
15. Schiaffino, S., and C. Reggiani. 1994. Myosin isoforms in mammalian skeletal muscle. *J. Appl. Physiol.* 76:371–423.
16. Fitzsimons, R. B., and J. F. Hoh. 1983. Myosin isoenzymes in fast-twitch and slow-twitch muscles of normal and dystrophic mice. *J. Physiol.* 343:539–550.
17. Karatzaferi, C., K. Franks-Skiba, and R. Cooke. 2007. The inhibition of shortening velocity of skinned skeletal muscle fibers in conditions that mimic fatigue. *Am. J. Physiol. Regul. Integr. Comp. Physiol.* n press 10.1152/ajpregu.00541.2007.
18. Lännergren, J. 1978. The force-velocity relation of isolated twitch and slow muscle fibres of *Xenopus laevis*. *J. Physiol.* 283:501–521.
19. Edman, K. A. P., and J. Hwang. 1977. The force-velocity relationship in vertebrate muscle fibres at varied tonicity of the extracellular medium. *J. Physiol.* 269:255–272.
20. Julian, F. J., L. Rome, and G. Stephenson. 1986. The maximum speed of shortening in living and skinned frog muscle fibres. *J. Physiol.* 370: 181–199.
21. Edman, K. A. P., L. A. Mulieri, and B. Scubon-Mulieri. 1976. Non-hyperbolic force-velocity relationship in single muscle fibres. *J. Physiol.* 98:143–156.
22. Edman, K. A. P. 1979. The velocity of unloaded shortening and its relation to sarcomere length and isometric force in vertebrate muscle fibres. *J. Physiol.* 291:143–159.
23. Vandenboom, R., D. R. Claflin, and F. J. Julian. 1998. Effects of rapid shortening on rate of force regeneration and myoplasmic $[Ca^{2+}]$ in intact frog skeletal muscle fibres. *J. Physiol.* 511:171–180.
24. Julian, F. J., and R. L. Moss. 1981. Effect of calcium and ionic strength on shortening velocity and tension development in frog skinned muscle fibres. *J. Physiol.* 311:179–199.
25. Westerblad, H., J. D. Bruton, and J. Lännergren. 1997. The effect of intracellular pH on contractile function of intact, single fibres of mouse muscle declines with increasing temperature. *J. Physiol.* 500: 193–204.
26. van Deutekom, C. T., and G.-J. B. van Ommen. 2003. Advances in Duchenne muscular dystrophy gene therapy. *Nat. Rev. Genet.* 4:774–783.
27. Campbell, K. P. 1995. Three muscular dystrophies: loss of cytoskeleton-extracellular matrix linkage. *Cell.* 80:675–679.
28. Durbeej, M., and K. P. Campbell. 2002. Muscular dystrophies involving the dystrophin-glycoprotein complex: an overview of current mouse models. *Curr. Opin. Genet. Dev.* 12:349–361.
29. Kumar, A., N. Khandelwal, R. Malya, M. B. Reid, and A. M. Boriek. 2004. Loss of dystrophin causes aberrant mechanotransduction in skeletal muscle fibers. *FASEB J.* 18:102–113.
30. Divet, A., A.-M. Lompre, and C. Huchet-Cadiou. 2005. Effect of cyclopiazonic acid, an inhibitor of the sarcoplasmic reticulum ATPase, on skeletal muscle from normal and mdx mice. *Acta Physiol. Scand.* 184:173–186.
31. Wang, X., N. Weisleder, C. Collet, J. Zhou, Y. Chu, Y. Hirata, X. Zhao, Z. Pan, H. Brotto, H. Cheng, and J. Ma. 2005. Uncontrolled calcium sparks act as a dystrophic signal for mammalian muscle. *Nat. Cell Biol.* 7:525–530.
32. Woods, C. E., D. Novo, M. DiFranco, J. Capote, and J. L. Vergara. 2005. Propagation in the transverse tubular system and voltage dependence of calcium release in normal and mdx mouse muscle fibres. *J. Physiol.* 568:867–880.
33. Friedrich, O., M. Both, J. M. Gillis, J. S. Chamberlain, and R. H. A. Fink. 2004. Mini-dystrophin restores L-type calcium currents in skeletal muscle of transgenic mdx mice. *J. Physiol.* 555:251–265.
34. Yeung, E. W., N. P. Whitehead, T. M. Suchyna, P. A. Gottlieb, F. Sachs, and D. G. Allen. 2005. Effects of stretch-activated channel blockers on $[Ca^{2+}]_i$ and muscle damage in the mdx mouse. *J. Physiol.* 562:367–380.
35. Bulfield, G., W. G. Siller, P. A. L. Wight, and K. J. Moore. 1984. X chromosome-linked muscular dystrophy (mdx) in the mouse. *Proc. Natl. Acad. Sci. USA.* 81:1189–1192.
36. Watchko, J. F., T. L. O'Day, and E. P. Hoffman. 2002. Functional characteristics of dystrophic skeletal muscle: insights from animal models. *J. Appl. Physiol.* 93:407–417.
37. Petrof, B. J., J. B. Shrager, H. H. Stedman, A. M. Kelly, and H. L. Sweeney. 1993. Dystrophin protects the sarcolemma from stresses developed during muscle contraction. *Proc. Natl. Acad. Sci. USA.* 90: 3710–3714.
38. Moens, P., P. H. W. W. Baatsen, and G. Marechal. 2003. Increased susceptibility of EDL muscles from mdx mice to damage induced by contractions with stress. *J. Muscle Res. Cell Motil.* 14:446–451.
39. Lowe, D. A., B. O. Williams, D. D. Thomas, and R. W. Grange. 2006. Molecular and cellular contractile dysfunction of dystrophic muscle from young mice. *Muscle Nerve.* 34:92–100.
40. Lynch, G. S., R. T. Hinkle, J. S. Chamberlain, S. V. Brooks, and J. A. Faulkner. 2001. Force and power output of fast and slow skeletal muscles from mdx mice 6–28 months old. *J. Physiol.* 535:591–600.
41. Coirault, C., F. Lambert, S. Marchand-Adam, P. Attal, D. Chemla, and Y. Lecarpentier. 1999. Myosin molecular motor dysfunction in dystrophic mouse diaphragm. *Am. J. Physiol.* 277:1170–1176.
42. Harper, S. Q., M. A. Hauser, C. DelloRusso, D. Duan, R. W. Crawford, S. F. Phelps, H. A. Harper, A. S. Robinson, J. F. Engelhardt, S. V. Brooks, and J. S. Chamberlain. 2002. Modular flexibility of dystrophin: implications for gene therapy of Duchenne muscular dystrophy. *Nat. Med.* 8:253–261.
43. Phelps, S., M. A. Hauser, N. M. Cole, J. A. Rafael, R. T. Hinkle, J. A. Faulkner, and J. S. Chamberlain. 1995. Expression of full-length and truncated dystrophin mini-genes in transgenic mdx mice. *Hum. Mol. Genet.* 4:1251–1258.
44. Gregorevic, P., M. J. Blankinship, J. M. Allen, R. W. Crawford, L. Meuse, D. G. Miller, D. W. Russel, and J. S. Chamberlain. 2004. Systemic delivery of genes to striated muscles using adeno-associated viral vectors. *Nat. Med.* 10:828–834.
45. Friedrich, O., J. S. Chamberlain, and R. H. A. Fink. 2005. Unloaded speed of shortening in intact single wt, mdx and mini-dystrophin (MinD) expressing murine skeletal muscle fibers under voltage-clamp conditions. *J. Muscle Res. Cell Motil.*, 26:84. (Abstr.)
46. Friedrich, O., T. Ehmer, and R. H. A. Fink. 1999. Calcium currents during contraction and shortening in enzymatically isolated murine skeletal muscle fibres. *J. Physiol.* 517:757–770.
47. Friedrich, O., T. Ehmer, D. Uttenweiler, M. Vogel, P. Barry, and R. H. A. Fink. 2001. Numerical analysis of Ca^{2+} depletion in the transverse tubular system (TTS) of mammalian muscle. *Biophys. J.* 80:2046–2055.
48. Friedrich, O., K. R. Kress, H. Ludwig, and R. H. A. Fink. 2002. Membrane ion conductances of mammalian skeletal muscle in the post-decompression state after high pressure treatment. *J. Membr. Biol.* 188: 1–12.
49. Laemmli, U. K. 1970. Cleavage of structural proteins during the assembly of the head of bacteriophage. *Nature.* 227:680–685.
50. Agbulut, O., Z. Li, V. Mouly, and G. S. Butler-Browne. 1996. Analysis of skeletal and cardiac muscle from desmin knock-out and normal mice by high resolution separation of myosin heavy-chain isoforms. *Biol. Cell.* 88:131–135.
51. Delbono, O., and E. Stefani. 1993. Calcium transients in single mammalian skeletal muscle fibres. *J. Physiol.* 463:689–707.
52. Hollingworth, S., M. Zhao, and S. M. Baylor. 1996. The amplitude and time course of the myoplasmic free $[Ca^{2+}]$ transient in fast-twitch fibres of mouse muscle. *J. Gen. Physiol.* 108:455–469.
53. Gonzalez-Serratos, H., R. Valle-Aguilera, D. A. Lathrop, and M. C. Garcia. 1982. Slow inward calcium currents have no obvious role in muscle excitation-contraction coupling. *Nature.* 298:292–294.
54. Bozzo, C., L. Stevens, L. Toniolo, Y. Mounier, and C. Reggiani. 2003. Increased phosphorylation of myosin light chain associated with slow-

to-fast transition in rat soleus. *Am. J. Physiol. Cell Physiol.* 285:C575–C583.

55. Nyitrai, M., R. Rossi, N. Adamek, M. A. Pellegrino, R. Bottinelli, and M. A. Geeves. 2006. What limits the velocity of fast-skeletal muscle contraction in mammals? *J. Mol. Biol.* 355:432–442.
56. Donaldson, P. L., and K. G. Beam. 1983. Calcium currents in a fast-twitch skeletal muscle of the rat. *J. Gen. Physiol.* 82:449–468.
57. Garcia, J., K. McKinley, S. H. Appel, and E. Stefani. 1992. Ca^{2+} current and charge movement in adult single human skeletal muscle fibres. *J. Physiol.* 454:183–196.
58. Stephenson, D. G., and D. A. Williams. 1985. Temperature-dependent calcium sensitivity changes in skinned muscle fibres of rat and toad. *J. Physiol.* 360:1–12.
59. Telley, I. A., J. Denoth, E. Stüssi, G. Pfitzer, and R. Stehle. 2006. Half-sarcomere dynamics in myofibrils during activation and relaxation studied by tracking fluorescent markers. *Biophys. J.* 90:514–530.
60. Podolsky, R. J., and A. Nolan. 1973. Muscle contraction transients, cross-bridge kinetics and the Fenn-effect. *Cold Spring Harb. Symp. Quant. Biol.* 37:661–668.
61. Roots, H., G. W. Offer, and K. W. Ranatunga. 2007. Comparison of the tension responses to ramp shortening and lengthening in intact mammalian muscle fibres: crossbridge and non-crossbridge contributions. *J. Muscle Res. Cell Motil.* 28:123–139.
62. Ranatunga, K. W. 1982. Temperature-dependence of shortening velocity and rat of isometric tension development in rat skeletal muscle. *J. Physiol.* 329:465–483.
63. Ranatunga, K. W. 1984. The force-velocity of rat fast- and slow-twitch muscles examined at different temperatures. *J. Physiol.* 351: 517–529.
64. Edman, K. A. P. 2006. Contractile properties of mouse single muscle fibers, a comparison with amphibian muscle fibers. *J. Exp. Biol.* 208: 1905–1913.
65. Barclay, C. J., J. K. Constable, and C. L. Gibbs. 1993. Energetics of fast- and slow-twitch muscles of the mouse. *J. Physiol.* 472:61–80.
66. Bottinelli, R., M. Canepari, M. A. Pellegrino, and C. Reggiani. 1996. Force-velocity properties of human skeletal muscle fibres: myosin heavy chain isoform and temperature dependence. *J. Physiol.* 495:573–586.
67. Asmussen, G., G. Beckers-Bleukx, and G. Marechal. 1994. The force-velocity relation of rabbit inferior oblique muscle; influence of temperature. *Pflugers Arch.* 426:542–547.
68. Petrof, B. J., H. H. Stedman, J. B. Shrager, J. Eby, H. L. Sweeney, and A. M. Kelly. 1993. Adaptations in myosin heavy chain expression and contractile function in dystrophic mouse diaphragm. *Am. J. Physiol. Cell Physiol.* 265:C834–C841.
69. Sugimoto, S., H. Takenaka, S. Yamashita, S. Matsukura, and M. Hamada. 1990. Kinetic properties and isozyme composition of myosin in the mdx mutant mouse. *J. Neurol. Sci.* 97:207–219.
70. Wolff, A. V., A. K. Niday, K. A. Voelker, J. A. Call, N. P. Evans, K. P. Granata, and R. W. Grange. 2006. Passive mechanical properties of maturing extensor digitorum longus are not affected by lack of dystrophin. *Muscle Nerve.* 34:304–312.